PHOTONICS Research

High-speed silicon photonic Mach–Zehnder modulator at 2 μm

Xi Wang,[1,†] Weihong Shen,[2,†] Wenxiang Li,[1] Yingjie Liu,[1] Yong Yao,[1] Jiangbing Du,[2,3] Qinghai Song,[1] and Ke Xu[1,4]

[1]Department of Electronic & Information Engineering, Harbin Institute of Technology, Shenzhen 518055, China
[2]State Key Laboratory of Advanced Optical Communication Systems and Networks, Shanghai Jiao Tong University, Shanghai 200240, China
[3]e-mail: dujiangbing@sjtu.edu.cn
[4]e-mail: kxu@hit.edu.cn

Received 9 December 2020; revised 26 January 2021; accepted 1 February 2021; posted 2 February 2021 (Doc. ID 417107); published 24 March 2021

Recently, 2-μm wave band has gained increasing interest due to its potential application for next-generation optical communication. But the development of 2-μm optical communications is substantially hampered by the modulation speed due to the device bandwidth constraints. Thus, a high-speed modulator is highly demanded at 2 μm. Motivated by this prospect, we demonstrate a high-speed silicon Mach–Zehnder modulator for a 2-μm wave band. The device is configured as a single-ended push–pull structure with waveguide electrorefraction via the free carrier plasma effect. The modulator was fabricated via a multiproject wafer shuttle run at a commercial silicon photonic foundry. The modulation efficiency of a single arm is measured to be 1.6 V · cm. The high-speed characterization is also performed, and the modulation speed can reach 80 Gbit/s with 4-level pulse amplitude modulation (PAM-4) formats.

https://doi.org/10.1364/PRJ.417107

1. INTRODUCTION

The continuously increasing demands for data capacity have been a primary concern in the fiber optical communication community. Multiple degrees of freedom, such as wavelengths, guiding modes, polarizations, and fiber cores, have been extensively exploited to maximize the transmission data capacity [1–5]. For all those techniques, the fundamental limit of fiber capacity is still approaching. The proposal for 2-μm optical communications offers an approach to circumvent the barriers between demands and state-of-the-art transmission techniques [6]. Owing to the much broader gain bandwidth of thulium-doped fiber amplifier (TDFA), a 2-μm wavelength range is potentially capable of supporting more wavelength channels than a 1.55-μm communication band [7]. In addition, the fiber attenuation can be optimized to 0.1 dB/km via a hollow core structure [8]. Experimental results for high-speed transmission have been demonstrated by several groups via discrete packaged components [9–16], but the current challenges associated with high-speed integrated modulators [17–20] and photodetectors still exist [6].

Given the fact that the well-established silicon photonics silicon-on-insulator (SOI) platform is transparent to 2-μm wavelengths, photonic integration at 2 μm is expected to prove a boon to device performance at 2 μm. Recently, growing research efforts have been devoted to building a comprehensive 2-μm wave band compatible library of optical components on silicon, such as grating couplers [21], resonators [22], arrayed waveguide gratings [23], modulators [24–26], photodetectors [27–29], switches [30], and mode multiplexers [31]. Though various functional elements have been demonstrated, the lack of high-speed and advanced modulators significantly hampers the progress of 2-μm optical communications. In fact, modulation in silicon waveguides offers intrinsic advantages such as a stronger free-carrier dispersion effect and weaker two-photon absorption compared with the C-band. The free-carrier modulation effect in silicon was first reported at 2-μm band with 3 Gbit/s, where the lumped electrode, parasite resistance, and capacitance limit the modulation speed [24]. More recently, the traveling-wave Mach–Zehnder modulators (MZMs) have been demonstrated, and the reported modulation speeds were 20 Gbit/s [25] and 50 Gbit/s [26]. Possibly due to the bandwidth, linearity, and efficiency constraints, multilevel modulation with advanced formats has not yet been achieved for 2-μm silicon modulators.

In this paper, we demonstrate a high-speed silicon MZM operated at 2-μm wave band. The device is designed in a single-ended push–pull configuration and is fabricated at a standard silicon photonic foundry. For the first time, to our knowledge, we demonstrate multilevel modulation in a silicon waveguide at 2-μm. A modulation speed of 80 Gbit/s using PAM-4 format is achieved, which is a record data rate.

2. MODULATOR DESIGN AND FABRICATION

The modulator is designed on a standard SOI substrate with 220 nm top silicon and 2-μm buried oxide. The MZM is configured in a single-end push–pull structure [20,32], and the cross-section schematic diagram is shown in Fig. 1. We first perform optical mode analysis by calculating the effective index of the waveguide under different widths. It can be seen from Fig. 2(a) that increasing the waveguide width will increase the effective refractive index of the waveguide. When it is higher than the single-mode cutoff condition, a multimode condition will be introduced. As shown in Fig. 2(b), the optical loss can be reduced while the waveguide width increases. On the other hand, wider waveguide has less optical loss caused by the roughness of the waveguide sidewall. To avoid a higher-order mode while maintaining low loss, the waveguide width is chosen to be 600 nm. The numerically calculated quasi-TE mode profiles are shown in the inset of Fig. 2(a). The corresponding n_{eff} is estimated as 2.33, and the simulated waveguide loss is 0.17 dB/cm.

It is well known that the modulation in silicon waveguides mainly relies on the free-carrier dispersion effect. Both the real part and the imaginary part of the refractive index vary with the carrier concentration in the waveguide. This effect was quantitatively characterized in the 2-μm spectral range, and the results indicate the following relationship [33]:

$$\Delta n = n_{\text{Ap}}(\Delta P)^{n_{\text{Ep}-}} + n_{\text{An}}(\Delta N)^{n_{\text{En}}}, \tag{1}$$

$$\Delta \alpha = \alpha_{\text{Ap}}(\Delta P)^{\alpha_{\text{Ep}}} + \alpha_{\text{An}}(\Delta N)^{\alpha_{\text{En}}}, \tag{2}$$

where Δn is the change in refractive index, $\Delta \alpha$ is the change in absorption coefficient, ΔP is the variation of hole concentration, and ΔN is the change in electron concentration. The free-carrier dispersion and absorption coefficients at 2-μm wave band are summarized in Table 1.

The two waveguide arms of the Mach–Zehnder interferometer are designed in parallel and share a common slab waveguide. As shown by Fig. 1, the two active waveguides are embedded with serial positive-negative-positive (PNP) junctions. The two junctions are identical and in a back-to-back configuration. The center regions of the rib waveguides are lightly doped with boron and phosphorus, with a doping level of 8×10^{17} cm^{-3} and 4×10^{17} cm^{-3}, respectively. To lower the contact resistance, the waveguide slab for electrodes is heavily doped with P++ (1×10^{19} cm^{-3}) and N++ (1×10^{19} cm^{-3}). The connecting part between the lightly doped and heavily doped regions is doped with an intermediate level of 2×10^{18} cm^{-3} and 2×10^{18} cm^{-3} for P+ and N+, respectively. From Table 1, it is easy to find a stronger free-carrier dispersion effect resulting from the hole. Thus, the P-doped width is designed to be larger than the N-doped region. We define a junction offset as the difference between the P-doped width and the N-doped width, i.e., $W_p - W_n$, as shown in Fig. 1. By calculation of the loss and modulation length required to achieve π phase shift, we first look into the junction offset effect, as shown in Figs. 3(a) and 3(b). To consider both the loss and modulation efficiency with a balanced view, a junction offset is chosen to be 50 nm to make the trade-off.

To avoid the absorption loss from the doped region, we also optimize the separation between the waveguide and the electrodes by investigation of the loss and modulation efficiency under different gap distances. An intermediately doped region (N+) is designed to buffer between the waveguide and the electrode. The detailed parameters can be found in Fig. 1. The simulation results are plotted in Figs. 3(c) and 3(d). Though the intermediately doped slab has much weaker absorption than the electrode, a gap distance of 300 nm is chosen to ensure the loss level is below 2 dB/cm. This effect is much more significant for a heavily doped region. The loss can be substantially reduced when the gap distance becomes larger than 500 nm, even though too much separation between the heavily doped region and the waveguide is not suggested, since the serial resistance increases with the separation. Lower resistance is also desirable for larger bandwidth, which is mainly limited to the

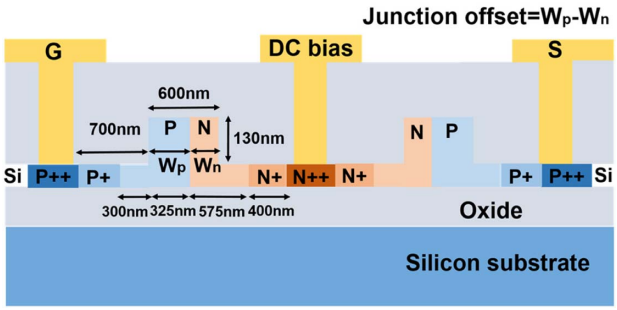

Fig. 1. Cross-sectional schematic diagram of the MZM's active arms.

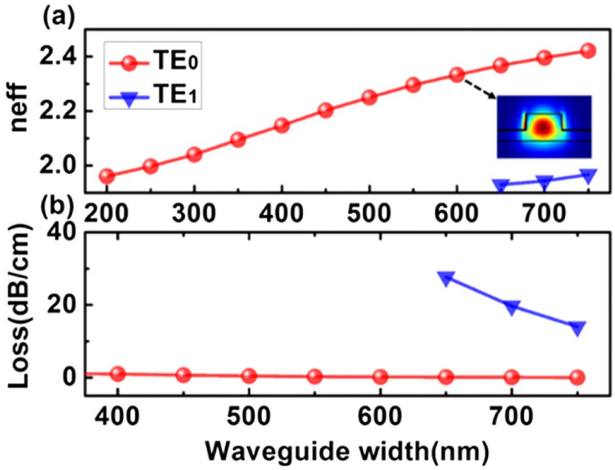

Fig. 2. (a) Mode analysis of a rib waveguide with 90 nm slab thickness; the inset is the quasi-TE mode profile; (b) simulated optical loss at wavelength of 1950 nm.

Table 1. Free-Carrier Dispersion and Absorption Coefficients

Dispersion Coefficients	n_{Ap} -2.28×10^{-18}	n_{Ep} 0.841	n_{An} -1.91×10^{-21}	n_{En} 0.992
Absorption coefficients	α_{Ap} 6.21×10^{-20}	α_{Ep} 1.119	α_{An} 3.22×10^{-20}	α_{En} 1.149

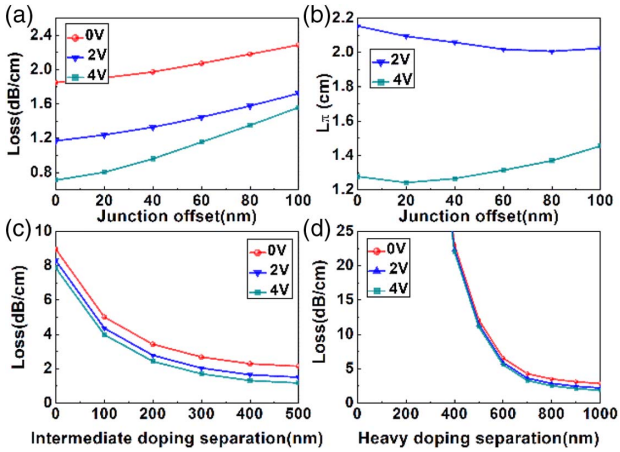

Fig. 3. (a) Loss performance under different PN junction offsets at the voltage of 0 V, 2 V, and 4 V; (b) relationship between L_π and PN junction offset under a voltage of 2 V and 4 V, respectively; (c) and (d) loss versus intermediate doping separation and heavy doping separation with a voltage of 0 V, 2 V, and 4 V, respectively.

resistance-capacitance (RC) constant. Thus, the finalized gap distance is determined to be 700 nm, which corresponds to a loss level of ~3 dB/cm. This is an intuitive trade-off determination according to the above analysis. We also notice that a slight loss reduction can be observed for both cases, which is due to the expansion of the depletion width.

Given the optimized waveguide design with all the above parameters, the modulator length is chosen to be 2 mm. The carrier distribution in the waveguide under different voltages is numerically simulated via the finite-element method. A reverse bias depletes the carriers from the waveguide center, which results in a change in refractive index. This is verified by simulations of carrier distribution and calculations of the depletion width under different reverse biases, as shown in Fig. 4. The depletion width doubles when 2 V reverse bias is applied to the positive-negative (PN) junction. Since the depletion region at the waveguide center has a large overlap with the optical mode, the refractive index can be effectively modified by the carrier density change. As shown by the inset of Fig. 4, an obvious expansion of the depletion region can be observed as the reverse bias is increased.

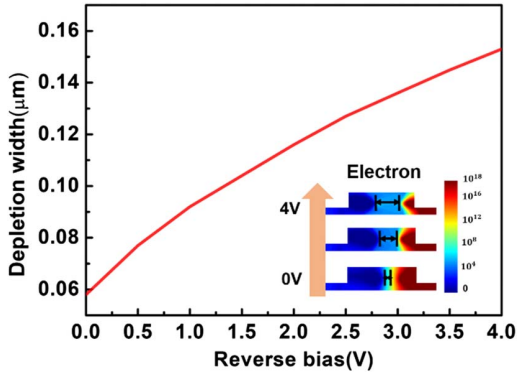

Fig. 4. Depletion width as a function of reverse bias. The inset is the distribution of electrons in the waveguide with a voltage of 0 V, 2 V, and 4 V, respectively.

The weak free-carrier dispersion effect in silicon leads to a very long active length to accumulate the amount of phase modulation. The millimeter scale of the modulator length could hardly operate at several tens of gigahertz via lumped electrodes due to the RC limitation and walk-off between RF and optical signals. To overcome this issue, the electrodes could be designed in a traveling-wave configuration, where the RF signal is copropagating in parallel with the optical wave in the silicon waveguide. The group index of silicon optical waveguide with a width of 600 nm is as high as 3.716 at 2 μm, which results in a much slower group velocity of the optical wave than the RF signal. Hence, a T-rail traveling-wave electrode is designed and optimized. The schematic diagram of the electrodes is shown in Fig. 5(a). Compared with a conventional coplanar strip (CPS) electrode, a T-rail electrode can increase the inductance while keeping the capacitance unchanged. Therefore, the microwave refractive index can be effectively increased to match the optical wave without sacrificing the modulation speed. The electrode optimization process involves a balanced consideration of electrode RF loss minimization, impedance matching, and group index matching [32]. The electrode parameters are finalized to be as follows: $W_1 = 120$ μm, $W_2 = 10$ μm, $H = 12$ μm, $G = 10$ μm, $P = 50$ μm, $L = 47$ μm, and $t = 2$ μm. Based on this electrode design, we perform the finite-element method simulations of unloaded transmission line to obtain the S parameters, which are plotted in Fig. 5(b).

Then, the simulated S parameters are converted to ABCD parameters using the formulation summarized in Refs. [32,34] to derive the RF attenuation, effective index, and characteristic impedance, as shown in Figs. 6(a), 6(b) and 6(c), respectively. It can be seen that RF attenuation increases at higher frequency, while the microwave index decreases to a constant value of 3.1. It means that a high-frequency regime leaves us with the difficulty of group velocity matching. Also, the modulation efficiency drops significantly at higher bit rates. The characteristic impedance is simulated to be 57.54 Ω at the frequency of 30 GHz, which is close to 50 Ω. At 30 GHz, the microwave loss is 0.64 dB/mm, and the microwave refractive index is 3.1. It should be noted that the microwave refractive index of this T-rail electrode structure is much higher than that of the traditional CPS. This design is expected to improve the modulation bandwidth. We obtain the electro-optic (EO) bandwidth by

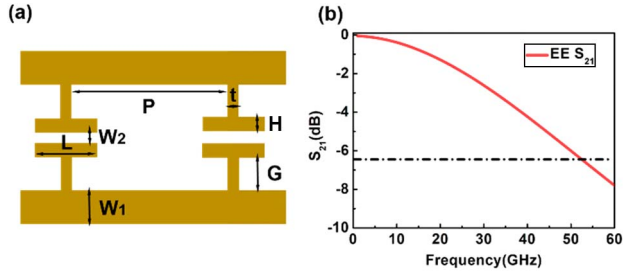

Fig. 5. (a) Two-dimensional schematic diagram of T-shaped rail electrode structure; (b) electro-electro (EE) S_{21} parameters of T-shaped traveling-wave electrode.

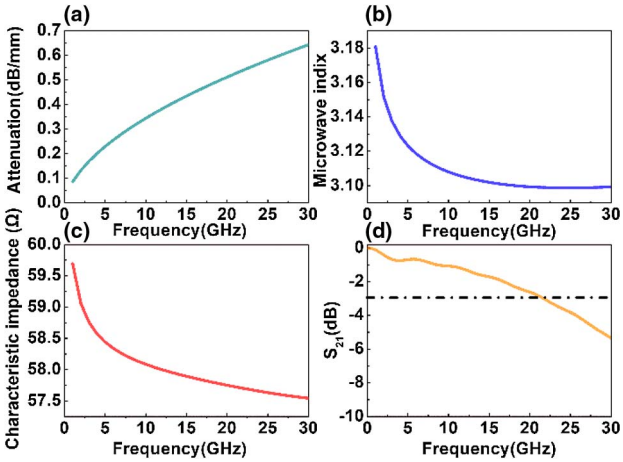

Fig. 6. Simulated frequency dependent (a) microwave attenuation, (b) microwave index, (c) characteristic impedance, and (d) EO S_{21} parameters.

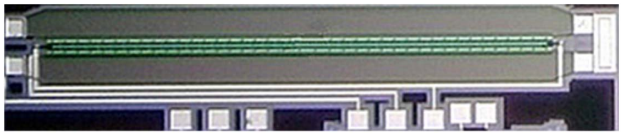

Fig. 7. Optical microscope image of the traveling-wave MZM.

simulating the EO response of the device. The EO S_{21} parameters are shown in Fig. 6(d), which indicates a 3-dB EO bandwidth of 21.7 GHz.

Based on the above modulator design, the device is fabricated via a standard silicon photonic multiproject wafer shuttle run provided by AMF Singapore. The microscope image of the fabricated MZM is shown in Fig. 7. The phase shifter is incorporated in both arms of the MZM to form a push–pull structure and to balance the loss. A multimode interferometer (MMI) is designed at 2 μm to equally split the incident wave into two arms. An edge coupler is used as an interface between the silicon waveguide and the SM-1950 fiber. The measured coupling loss is about 2.5 dB/facet. Compared with the grating coupler, the edge coupler has lower coupling loss, less polarization dependency, and broader bandwidth. The RF signals are launched from the left-hand side of the ground-signal (GS) pads and travel through the T-rail electrodes until reaching the right-hand side GS pads, which are terminated with an on-chip 50 Ω resistor.

3. STATIC MEASUREMENTS

We first measure the DC response of the modulator. A narrow linewidth laser with an output wavelength of 1952 nm is used as the light source. A polarization controller is made of 5-m-long SM-1950 single-mode fiber and is used to ensure polarization alignment. A lensed fiber is used to focus the light into the edge coupler with a matched mode field diameter. The output from the chip is measured by an InGaAs power meter. DC voltage is applied onto the DC electrode pads via a pair of DC probes.

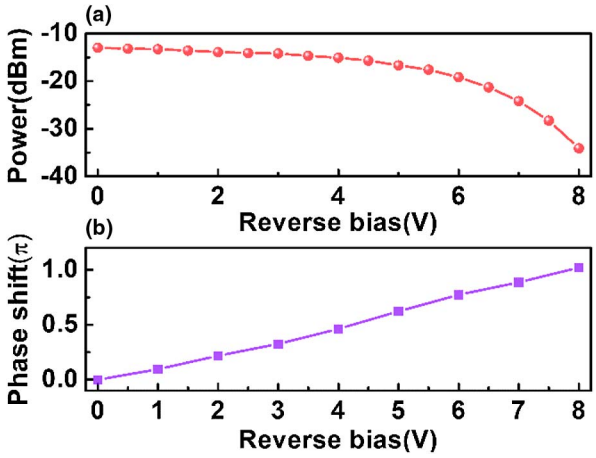

Fig. 8. (a) Measured optical transmission and (b) phase shift as functions of reverse bias.

The measured total insertion loss of the MZM is 15 dB at its peak transmission, including a 5 dB coupling loss. Since the laser is not wavelength-tunable, we perform a single wavelength measurement by recording the output power under different bias voltages. The results are plotted in Fig. 8(a). The output power varies periodically with the bias, which is due to the interference. At zero bias, it is very close to the transmission peak, while a valley occurs with 8 V bias. It means that the applied voltage provides a π phase difference between the two interference arms. Thus, the V_π can be estimated to be 8 V, and the corresponding $V_\pi \cdot L$ is 1.6 V · cm. Owing to the balance of propagation constants in the two arms, the measured extinction ratio of the modulator is 22 dB. As shown in Fig. 8(b), we also calculate the corresponding phase shift under different bias voltages, which further confirms the free-carrier dispersion effect.

4. HIGH-SPEED MEASUREMENTS

As shown in Fig. 9, the experimental setup for the high-speed test is similar to the DC characterization. To compensate for the chip loss, a TDFA is used to boost the optical power. The high-speed pseudorandom binary sequence (PRBS) is generated from an arbitrary waveform generator (AWG, Keysight 8195A) and amplified by an electrical amplifier. Then, a

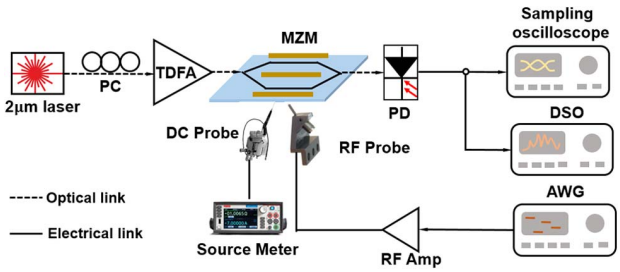

Fig. 9. Schematic diagram of the high-speed measurement setup. PD, photodetector; DSO, digital storage oscilloscope; AWG, arbitrary waveform generator; TDFA, thulium-doped fiber amplifier; PC, polarization controller.

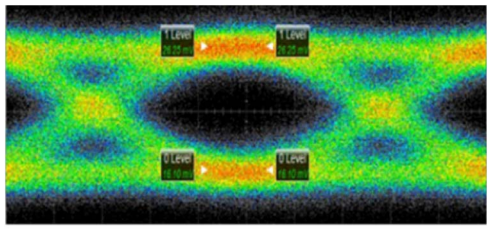

Fig. 10. Eye diagram for MZM at data rate of 30 Gbit/s with OOK modulation.

GS-type RF probe with 150-μm pitch is used to apply the electrical data to the traveling-wave electrodes. For the single-ended push–pull configuration, the DC bias electrode is the middle one right above the N++ region, and the biasing is done through an on-chip metal trace having a high inductance instead of external bias tees. The output of the modulator is received by a commercial high-speed InGaAs photodetector with a 3-dB bandwidth of 22 GHz. Then the electrical output of the photodetector is sent to an oscilloscope to measure the eye diagrams, or the real-time digital storage oscilloscope (DSO) with 160-GSa/s sampling rate for offline digital signal processing. The bit error rate (BER) is calculated after root raised cosine filtering and feed-forward equalization (FFE) are performed.

We perform the on–off keying (OOK) modulation first; the measured eye diagram is shown in Fig. 10. By driving the silicon modulator with 3.6 V PRBS signals at 30 Gbit/s, the incident receiver power is 1.5 mW. The measured eye diagram is wide open, with an extinction ratio of 2.1 dB. The excess noise mainly comes from the TDFA due to the lack of optical filter. This could have been improved if an optical amplifier with a lower noise figure and a high-performance optical filter were available. Then, we also try the PAM-4 modulation to increase the bit rate. The measured BER curves and eye diagrams of the PAM-4 modulation after FFE are shown in Fig. 11. The 60 Gbit/s modulated signals can achieve BER well below the forward error correction (FEC) limit of 3.8×10^{-3} with hard decision and 7% overhead. For 80 Gbit/s modulation, 0.92 mW receiver power is needed to lower the BER down

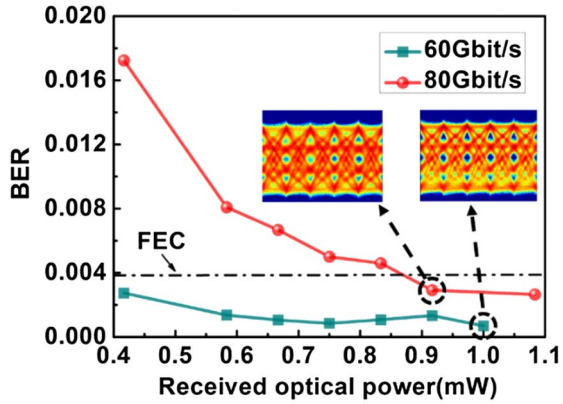

Fig. 11. BER curves at different modulation rates. Inset: the offline post-FFE eye diagrams of 80 Gbit/s (left) and 60 Gbit/s (right) PAM-4 signals.

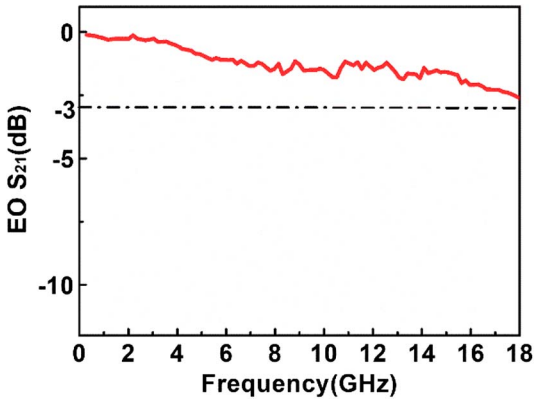

Fig. 12. Measured EO S_{21} response of the 2-μm MZM at −2 V DC bias.

to the FEC limit. This can be verified by the eye diagrams of both cases, which are shown in the inset of Fig. 11. It can be seen that the eye opening degrades significantly by increasing the data rate to 80 Gbit/s.

Finally, we measure the frequency response of the modulator by normalizing the response of the cables and the photodetectors. Since the RF probe has a 3-dB bandwidth of 40 GHz, we assume it has negligible impact on the measurement result. But the frequency range of the measurement is limited by the bandwidth of the vector network analyzer (Keysight E5063A), which is only 18 GHz. As shown in Fig. 12, it can be seen that the actual 3-dB bandwidth of the silicon modulator (biased at −2 V) should be beyond 18 GHz.

5. CONCLUSION

To summarize, we have experimentally demonstrated a silicon photonic MZM at 1950 nm with a single-ended push–pull configuration. The length of the modulator is 2 mm with a measured V_π of 8 V. The experimental results show that intensity modulation with a record speed of 80 Gbit/s via PAM-4 formats is achieved. The measured BER is below 3.8×10^{-3} under a receiver power of 0.92 mW. The modulation speed is limited by the bandwidth constraints of the testing system. The bandwidth of the modulator itself can be further optimized by better group velocity matching of the RF and optical signals. This work has improved the modulation speed of a silicon modulator in the 2 μm wave band, which is important to develop the optical communications in this spectral window.

Funding. National Natural Science Foundation of China (61875049, 61875124, 61935011); Science, Technology and Innovation Commission of Shenzhen Municipality (JCYJ2016042718380345, JCYJ20180306171923592, JCYJ20180507183418012, JSGG20190819175801678, KQJSCX20180328165451777).

Disclosures. The authors declare no conflicts of interest.

†These authors contributed equally to this work.

REFERENCES

1. B. Zhu, T. Taunay, M. Fishteyn, X. Liu, S. Chandrasekhar, M. Yan, J. Fini, E. Monberg, and F. Dimarcello, "112-Tb/s space-division multiplexed DWDM transmission with 14-b/s/Hz aggregate spectral efficiency over 76.8-km seven-core fiber," Opt. Express **19**, 16665–16671 (2011).
2. Z. Y. Chen, L. S. Yan, Y. Pan, L. Jiang, A. Yi, W. Pan, and B. Luo, "Use of polarization freedom beyond polarization-division multiplexing to support high-speed and spectral-efficient data transmission," Light Sci. Appl. **6**, e16207 (2017).
3. D. J. Richardson, J. Fini, and L. E. Nelson, "Space-division multiplexing in optical fibres," Nat. Photonics **7**, 354–362 (2013).
4. S. Randel, R. Ryf, A. Sierra, P. Winzer, A. Gnauck, C. Bolle, R. Essiambre, D. Peckham, A. McCurdy, and R. Lingle, "6×56-Gb/s mode division multiplexed transmission over 33-km few-mode fiber enabled by 6×6 MIMO equalization," Opt. Express **19**, 16697–16707 (2011).
5. L. Zhu, A. Wang, S. Chen, J. Liu, and J. Wang, "Orbital angular momentum mode multiplexed transmission in heterogeneous few-mode and multi-mode fiber network," Opt. Lett. **43**, 1894–1897 (2018).
6. R. Soref, "Enabling 2-μm communications," Nat. Photonics **9**, 358–359 (2015).
7. Z. Liu, Y. Chen, Z. Li, B. Kelly, R. Phelan, J. Carroll, T. Bradley, J. P. Wooler, N. V. Wheeler, A. M. Heidt, T. Richter, C. Schubert, M. Becker, F. Poletti, M. N. Petrovich, S. Alam, D. J. Richardson, and R. Slavik, "High-capacity directly modulated optical transmitter for 2-μm spectral region," J. Lightwave Technol. **33**, 1373–1379 (2015).
8. P. J. Roberts, F. Couny, H. Sabert, B. J. Mangan, D. P. Williams, L. Farr, M. W. Mason, and A. Tomlinson, "Ultimate low loss of hollow-core photonic crystal fibres," Opt. Express **13**, 236–244 (2005).
9. K. Xu, L. Sun, Y. Q. Xie, Q. H. Song, J. B. Du, and Z. Y. He, "Transmission of IM/DD signals at 2-μm wavelength using PAM and CAP," IEEE Photon. J. **8**, 7906407 (2016).
10. D. M. Kong, Y. Liu, Z. G. Ren, Y. M. Jung, M. H. Pu, K. Yvind, M. Galili, L. K. Oxenløwe, D. J. Richardson, and H. Hu, "Generation and coherent detection of 2-μm-band WDM-QPSK signals by on-chip spectral translation," in *Optical Fiber Communication Conference* (2020), paper M1I.4.
11. K. Xu, Q. Wu, Y. Xie, M. Tang, S. Fu, and D. Liu, "High speed single-wavelength modulation and transmission at 2-μm under bandwidth-constrained condition," Opt. Express **25**, 4528–4534 (2018).
12. M. N. Petrovich, F. Poletti, J. P. Wooler, A. M. Heidt, N. K. Baddela, Z. Li, D. R. Gray, R. Slavík, F. Parmigiani, N. V. Wheeler, J. R. Hayes, E. Numkam, L. G. Nielsen, B. Pálsdóttir, R. Phelan, B. Kelly, M. Becker, N. MacSuibhne, J. Zhao, F. C. G. Gunning, A. D. Ellis, P. Petropoulos, S. U. Alam, and D. J. Richardson, "First demonstration of 2-μm data transmission in a low-loss hollow core photonic bandgap fiber," Opt. Express **21**, 28559–28569 (2013).
13. Z. Li, A. M. Heidt, N. Simakov, Y. Jung, J. M. O. Daniel, S. U. Alam, and D. J. Richardson, "Diode-pumped wideband thulium-doped fiber amplifiers for optical communications in the 1800-2050 nm window," Opt. Express **21**, 26450–26455 (2013).
14. H. Zhang, N. Kavanagh, Z. Li, J. Zhao, N. Ye, Y. Chen, N. V. Wheeler, J. P. Wooler, J. R. Hayes, S. R. Sandoghchi, F. Poletti, M. N. Petrovich, S. U. Alam, R. Phelan, J. O'Carroll, B. Kelly, L. Grüner-Nielsen, D. J. Richardson, B. Corbett, and F. C. G. Gunning, "100 Gbit/s WDM transmission at 2-μm: transmission studies in both low-cost hollow core photonic bandgap fiber and solid core fiber," Opt. Express **23**, 4946–4951 (2015).
15. W. Shen, J. Du, L. Sun, C. Wang, Y. Zhu, K. Xu, B. Chen, and Z. He, "Low-latency and high-speed hollow-core fiber optical interconnection at 2-micron waveband," J. Lightwave Technol. **38**, 3874–3882 (2020).
16. W. Shen, P. Zeng, Z. Yang, D. Xia, J. Du, B. Zhang, K. Xu, Z. He, and Z. Li, "Chalcogenide glass photonic integration for improved 2-μm optical interconnection," Photon. Res. **8**, 1484–1490 (2020).
17. P. Dong, L. Chen, and Y. K. Chen, "High-speed low-voltage single-drive push-pull silicon Mach-Zehnder modulators," Opt. Express **20**, 6163–6169 (2012).
18. X. Xiao, H. Xu, X. Y. Li, Z. Y. Li, T. Chu, Y. D. Yu, and J. Z. Yu, "High-speed, low-loss silicon Mach–Zehnder modulators with doping optimization," Opt. Express **21**, 4116–4125 (2013).
19. S. Z. Shao, J. F. Ding, L. C. Zheng, K. H. Zou, L. Zhang, F. Zhang, and L. Yang, "Optical PAM-4 signal generation using a silicon Mach-Zehnder optical modulator," Opt. Express **25**, 23003–23013 (2017).
20. Y. Y. Zhou, L. J. Zhou, H. K. Zhu, C. Y. Wong, Y. D. Wen, L. Liu, X. W. Li, and J. P. Chen, "Modeling and optimization of a single-drive push–pull silicon Mach–Zehnder modulator," Photon. Res. **4**, 153–161 (2016).
21. J. Y. Li, Y. J. Liu, Y. Meng, K. Xu, J. B. Du, F. Wang, Z. Y. He, and Q. H. Song, "2-μm wavelength grating coupler, bent waveguide, and tunable microring on silicon photonic MPW," IEEE Photon. Technol. Lett. **30**, 471–474 (2018).
22. C. Luan, Y. Liu, Y. Ding, and H. Hu, "2-μm high-speed graphene electro-optic modulator based on silicon slot microring resonator," in *Conference on Lasers and Electro-Optics* (2020), paper jTh2F.34.
23. Y. Liu, Z. Li, D. Li, Y. Yao, J. Du, Z. He, and K. Xu, "Thermo-optic tunable silicon arrayed waveguide grating at 2-μm wavelength band," IEEE Photon. J. **12**, 4900308 (2020).
24. M. A. Camp, S. Assefa, D. M. Gill, T. Barwicz, S. M. Shank, P. M. Rice, T. Topuria, and W. J. Green, "Demonstration of electrooptic modulation at 2165 nm using a silicon Mach-Zehnder interferometer," Opt. Express **20**, 28009–28016 (2012).
25. W. Cao, D. Hagan, D. J. Thomson, M. Nedeljkovic, C. G. Littlejohns, A. Knights, S. Alam, J. J. Wang, F. Gardes, W. W. Zhang, S. H. Liu, K. Li, M. S. Rouifed, G. Xin, W. J. Wang, H. Wang, G. T. Reed, and G. Z. Mashanovich, "High-speed silicon modulators for the 2-μm wavelength band," Optica **5**, 1055–1062 (2018).
26. W. Li, M. Li, H. Zhang, Y. Zhang, H. Xie, X. Xiao, and K. Xu, "50 Gbit/s silicon modulator operated at 1950 nm," in *Optical Fiber Communication Conference* (2020), paper M1D.4.
27. J. Guo, J. Li, C. Liu, Y. Yin, W. Wang, Z. Ni, Z. Fu, H. Yu, Y. Xu, Y. Shi, Y. Ma, S. Gao, L. Tong, and D. Dai, "High-performance silicon-graphene hybrid plasmonic waveguide photodetectors beyond 1.55 μm," Light Sci. Appl. **9**, 29 (2020).
28. Y. Dong, W. Wang, S. Xu, D. Lei, X. Gong, X. Guo, H. Wang, S. Lee, W. Loke, S. Yoon, and Y. Yeo, "Two-micron-wavelength germanium-tin photodiodes with low dark current and gigahertz bandwidth," Opt. Express **25**, 15818–15827 (2017).
29. J. J. Ackert, D. J. Thomson, L. Shen, A. C. Peacock, P. E. Jessop, G. T. Reed, G. Z. Mashanovich, and A. P. Knights, "High-speed detection at two micrometres with monolithic silicon photodiodes," Nat. Photonics **9**, 393–396 (2015).
30. T. Yu, Y. J. Liu, Z. Y. Li, K. Xu, and J. B. Du, "Integrated thermo-optic switch for 2-μm spectral band," in *International Photonics and Optoelectronics Meeting* (2019), paper OTu2B.4.
31. S. Zheng, M. Huang, X. Cao, L. Wang, Z. Ruan, L. Shen, and J. Wang, "Silicon-based four-mode division multiplexing for chip-scale optical data transmission in 2-μm waveband," Photon. Res. **7**, 1030–1035 (2019).
32. D. Patel, S. Ghosh, M. Chagnon, A. Samani, V. Veerasubramanian, M. Osman, and D. V. Plant, "Design, analysis, and transmission system performance of a 41 GHz silicon photonic modulator," Opt. Express **23**, 14263–14287 (2015).
33. M. Nedeljkovic, R. Soref, and G. Mashanovich, "Free-carrier electrorefraction and electroabsorption modulation predictions for silicon over the 1–14 μm infrared wavelength range," IEEE Photon. J. **3**, 1171–1180 (2011).
34. D. Frickey, "Conversions between S, Z, Y, H, ABCD, and T parameters which are valid for complex source and load impedances," IEEE Trans. Microw. Theory Tech. **42**, 205–211 (1994).